Traffic 2012; **13:** 979–991

doi:10.1111/j.1600-0854.2012.01361.x

Interaction with a Kinesin-2 Tail Propels Choline Acetyltransferase Flow Towards Synapse

Aparna Sadananda†, Runa Hamid†, Harinath Doodhi, Debnath Ghosal, Mukul Girotra, Swadhin Chandra Jana and Krishanu Ray*

[1]*Department of Biological Sciences, Tata Institute of Fundamental Research, Mumbai, India*

**Corresponding author: Krishanu Ray, krishanu@tifr.res.in*

†*A. Sadananda and R. Hamid equally contributed to this article.*

Bulk flow constitutes a substantial part of the slow transport of soluble proteins in axons. Though the underlying mechanism is unclear, evidences indicate that intermittent, kinesin-based movement of large protein-aggregates aids this process. Choline acetyltransferase (ChAT), a soluble enzyme catalyzing acetylcholine synthesis, propagates toward the synapse at an intermediate, slow rate. The presynaptic enrichment of ChAT requires heterotrimeric kinesin-2, comprising KLP64D, KLP68D and DmKAP, in *Drosophila*. Here, we show that the bulk flow of a recombinant Green Fluorescent Protein-tagged ChAT (GFP::ChAT), in *Drosophila* axons, lacks particulate features. It occurs for a brief period during the larval stages. In addition, both the endogenous ChAT and GFP::ChAT directly bind to the KLP64D tail, which is essential for the GFP::ChAT entry and anterograde flow in axon. These evidences suggest that a direct interaction with motor proteins could regulate the bulk flow of soluble proteins, and thus establish their asymmetric distribution.

Key words: asymmetric distribution, bulk flow, choline acetyltransferase, *Drosophila*, kinesin-2, slow axonal transport

Received 22 November 2011, revised and accepted for publication 2 April 2012, uncorrected manuscript published online 4 April 2012, published online 26 April 2012

Neurons grow long extended axons with specialized enrichment of a number of different types of proteins at the presynaptic terminal. Pulse-chase experiments with radio-labeled amino acids showed that cytoskeletal elements and other soluble proteins are transported in bulk at two broadly classified rates in the axon, defined as slow component a (SCa, 0.1–1 mm/day) and slow component b (SCb, 2–10 mm/day). These are much slower than the rates (20–450 mm/day) of the membrane-bound vesicle movements (reviewed in 1). Cytoskeletal proteins (2,3), motors such as cytoplasmic dynein (4) and myosins (5), and a large number of soluble enzymes (6,7) are transported in the slow component. It is implicated in neurological disorders (8) and neuronal growth (9,10).

Slow axonal transport was assumed to occur in continuous bulk flow. In contrast, time lapse imaging of tissue cultured neurons, expressing fluorescence tagged proteins, revealed that filamentous and punctate forms of neurofilaments (11–14), and microtubules (MT) (15) propagate in the axon, in intermittent, rapid bursts. Many SCb proteins, such as synapsin-1, glyceraldehyde-3-phosphate dehydrogenase and α-synuclein (16), also move in a similar fashion, and the process is MT dependent (17). Also, oligomeric tubulin is reported to flow in a kinesin-dependent manner (18). Stochastic simulations and further data analysis indicated that prolonged pauses during the transport of soluble, protein aggregates could result in an overall slow rate in axons (19,20). Finally, a careful examination of axonal transport of CamKinase-IIa and synapsin-1 in cultured neurons revealed intricate particulate movements, within the spreading bulk of these two proteins. Physical modeling of the experimental data and numeric analysis suggested that a combination of occasional motor-driven movement of supramolecular complexes and intermittent diffusion generate the bulk flow of soluble proteins in axons (21).

Choline acetyltransferase (ChAT), a soluble and monomeric enzyme involved in acetylcholine (ACh) synthesis, is exclusively localized at the presynaptic compartment (22). It moves anterogradely in bulk at 1.25 mm/day in rat sciatic nerve axons (23). In *Drosophila*, ChAT immunoreactivity increases steadily at the neuropile region during the larval stages (24). Loss of ChAT activity in adult flies causes progressive paralysis in homozygous cha^{ts} mutants and total loss-of-function *cha* mutant larvae are unable to hatch (25,26). An early deficit in cholinergic brain function preceding the onset of the disease pathology is also implicated in many neurodegenerative disorders, such as Alzheimer's disease (27). Loss of ACh synthesis, as well as the ChAT and AChE activities at the synapse precede Aβ aggregation in mice models of Alzheimer's disease (28). In addition, aberrant ChAT transport in motor neurons is linked to the familial amyotrophic lateral sclerosis (29). Thus, understanding the mechanism of slow axonal transport of ChAT has gained prominence.

ChAT associates with kinesin-2 (24,29,30). The gradual synaptic enrichment of ChAT in the ventral ganglia (VG) of *Drosophila* larvae is MT dependent and requires the kinesin-2 family motor comprising KLP64D, KLP68D and DmKAP (24,31). However, the spatiotemporal resolution of the latter reports was low, which necessitated a further high-resolution analysis of ChAT transport dynamics in axons. We expected that ChAT would be packaged into macromolecular complexes and transported at a faster rate, commensurate with the rate of kinesin-2

movements. To test this hypothesis, we expressed a recombinant N-terminal Green Fluorescent Protein tagged ChAT (GFP::ChAT) in the cholinergic neurons of *Drosophila* larvae, and studied its transport properties and association with the kinesin-2 subunits *ex vivo*. The results described below suggest that packaging proteins into vesicles, or large macromolecular complexes, is not mandatory for their long-range transport and indicates that soluble proteins can be asymmetrically distributed inside a cell by directed flow, and maintained and regulated by molecular motors.

Results

Recombinant GFP::ChAT localizes in the synapses of cholinergic neurons

At first, we compared the tissue localization and the ability of the recombinant protein to bind kinesin-2. The soluble form of GFP::ChAT (Figure 1A), obtained from the head extracts of *Cha-GAL4>UAS-GFP::ChAT* flies, co-precipitated with KLP68D, which is a kinesin-2 motor subunit, but failed to co-precipitate KHC, the kinesin-1 motor subunit (Figure 1B). This demonstrated that the recombinant protein could selectively associate with the endogenous kinesin-2. The expression pattern of the recombinant protein in *Cha-GAL4>UAS-GFP::ChAT* embryos is similar to the endogenous ChAT (data not shown), but occurs with approximately a 2.5-h delay. It also rescued the cha^{ts1} recessive lethality (data not shown). Thus, we established that the recombinant protein is functionally equivalent to the endogenous one.

Further studies in the VG of the *Cha-GAL4>UAS-GFP::ChAT* larvae indicated that the recombinant GFP::ChAT could localize to the synapses of dorsal neuropile region (arrow, Figure 1C,D). In addition, it was present in the segmental nerve axons as well as in interneurons (arrowheads, Figure 1C,D). The GFP::ChAT fluorescence was much higher in the live VG preparations and a majority of that was extracted during the 0.3% tritonX-100 wash after fixation, indicating that most of the GFP::ChAT in these neurons is soluble. Furthermore, the fluorescence intensities in the cell bodies of interneurons progressively declined with a concomitant gain in the VG axons in older larvae (Figure 1E), suggesting that the protein undergoes dynamic re-localization in neurons during the larval stages.

Fluorescence recovery after photobleaching (FRAP) assay in the synapses and axons defined a brief period of GFP::ChAT transport

Endogenous ChAT progressively enriches in the neuropile in the 72–90-h interval after-egg-laying (AEL) and low levels of vinblastine treatment affect the process during 74–90 h AEL (24). FRAP study in the neuropile of VG preparations (Figure 2A), dissected from live *Cha-GAL4>UAS-GFP::ChAT* larvae, produced the most prominent recovery at 78 h AEL (Figures 2B and S1). It was significantly higher than those at other time-points. In comparison, the GFP recovery in the same area of *Cha-GAL4>UAS-GFP* VG was constitutive throughout the third instar stage (Figure S1). As we measured FRAP in isolated VG preparations, the flow could only arrive from the cortical cell bodies. Hence, we estimated the recovery profiles in the axons of the interneurons in the dorsal and ventral regions of the cortex at different stages. In a majority of such interneurons, the recovery occurred at 78 h AEL (Figure S2).

To analyze the process further, we measured FRAP at 10 frames/second and extended the bleached region-of-interest (ROI) length to 10 μm (Figure 2C). The fluorescence recovery was optimal under these conditions. This confirmed that GFP recovers at a significantly higher rate at the initial stage as compared to GFP::ChAT (Figure 2D). In addition, though the GFP recovery profiles were almost identical in the 77–79 h AEL period, the maximum GFP::ChAT recovery occurred at 78 h AEL (Figure 2D). Together, these suggested that GFP::ChAT entry and flow in the axon during the third instar larval stage is regulated. The FRAP study also revealed that on an average 31% of the GFP::ChAT recovery occurred in the first 3 seconds, and it went up to 41% of the pre-bleach values within 9 seconds. On the other hand, the GFP fluorescence recovered to a maximum of 62% of the pre-bleach values with 48% initial recovery under comparable conditions. The initial rate was 1.5-fold higher for GFP than that of GFP::ChAT while the subsequent recovery occurred at similar rates. We considered it a secondary accumulation effect. The GFP diffusion constant in the cytoplasm (30 μm^2/second), estimated using the Stokes-Einstein equation (see *Methods*), is almost 1.8 times higher than that of GFP::ChAT (17 μm^2/second). In addition, interaction with kinesin-2 and other proteins in axons could further reduce the GFP::ChAT propagation and account for its somewhat slower recovery. Contrary to expectations, however, the FRAP movies also indicated that GFP::ChAT gradually diffuses into the axon. There was no intricate particle kinetics observed during the recovery (Video S1), as reported for CaMKIIa earlier (21).

Endogenous as well as recombinant GFP::ChAT associates with the KLP64D tail

ChAT associates with kinesin-2 in *Drosophila* head extract (24,30) and mouse motor axons (29). Therefore, to understand the role of kinesin-2 in its transport, we determined the binding site of endogenous as well as GFP::ChAT on the kinesin-2 subunits. For this, we used recombinant tail and stalk fragments of the motor subunits as bait (Figure 3A). Of these, only the poly-histidine tagged KLP64D tail (His-KLP64DT) and its Glutathione *S*-transferase-tagged variant (GST-KLP64DT) could pull down ChAT and GFP::ChAT from the fly head extracts (Figure 3B). In addition, both GST-KLP64DT and GST-KIF3AT pulled down two different forms of rat ChAT (rChAT) from the sciatic nerve extract (Figure 3C). Interestingly, His-KLP64DT also pulled down recombinant rChAT from the *Escherichia coli* extract (Figure 3D), and

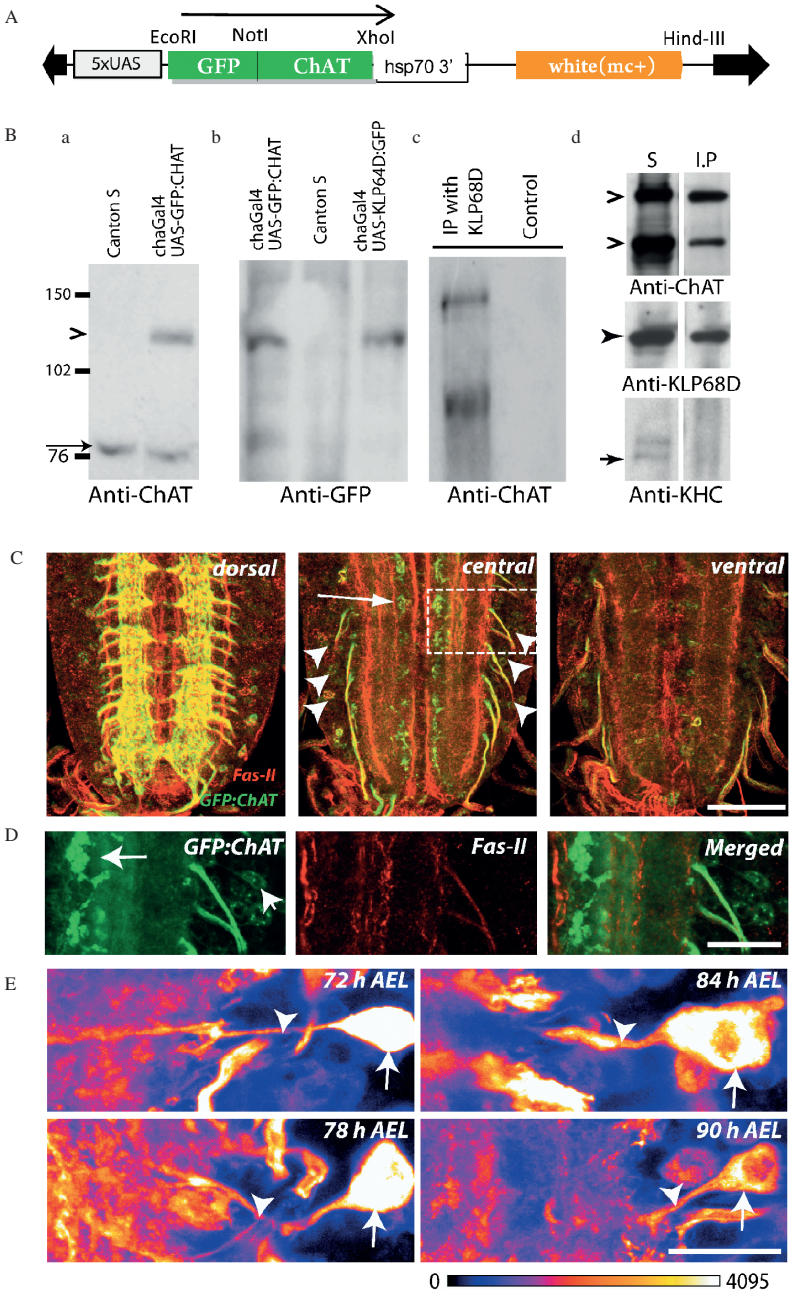

Figure 1: GFP::ChAT localization in cholinergic neurons. A) Schematic illustrates key coding elements and their organization within pUASt-GFP::ChAT transposon. Solid black arrows indicate the P-element LTRs. The GFP and ChAT coding fragments are inserted between the *Eco*RI/*Not*I and *Not*I/*Xho*I sites, respectively. Overriding open arrow indicates the direction of the GFP::ChAT expression, initiated from the 5xUAS elements at the 5′ end. B) Western blots of head extracts from wild-type and *Cha*-GAL4>UAS-GFP:ChAT flies stained with mAb4B1 (a) and rabbit polyclonal anti-GFP (b). The positions of 81 kDa endogenous ChAT (fine arrow) and the 108 kDa GFP:ChAT (open arrowhead) bands are indicated on the left margin. 108 kDa GFP::ChAT co-precipitated with purified anti-KLP68D along with the 81 kDa endogenous ChAT (c). However, both GFP::ChAT and endogenous ChAT failed to co-precipitate with kinesin heavy chain (KHC) in the immunoprecipitation using anti-ChAT antibody (d). C, D) GFP::ChAT localizations in the ventral ganglion (VG) of third instar larvae. Panels in (C) (left to right) indicate GFP::ChAT (green) localization and Fas II staining in the dorsal, central and ventral regions of the VG. Panel (D) shows an enlarged view of a lateral abdominal segment of VG marked by broken lines in (C). Arrows indicate the synapses of the lateral chordotonal neurons in the central neuropile region and the arrowhead indicates the cell bodies of cholinergic inter-neurons in the cortex. E) GFP::ChAT localization in the ventrolateral neurons (indicated by arrowheads in C) in isolated unfixed VG preparations from 72 h, 78 h, 84 h, and 90 h AEL larvae. The fluorescence intensities are presented according to a false color spectrum scale shown at the bottom right. Arrows indicate the cell bodies and arrowheads indicate the axons in each panel. Scale bar in (C) 50 μm, (D) and (E) 25 μm. LTR, Long Terminal Repeat; UAS, Upstream activation sequence.

a comparatively lower amount is co-purified with the truncated KLP64D tail (His-KLP64DTc), containing the conserved N-terminal part of the tail fragment (Figure 3D). The heterologous pull-down of rChAT with *Drosophila* KLP64D tail indicated that the interaction between kinesin-2 and ChAT is universal and highly conserved. Overall, the ChAT pull-down yields were relatively low at physiological ionic strength and eliminated at 400 mM KCl (data not shown). Therefore, the interaction is likely to be charge based and may occur through the conserved portion of the KIF3A/KLP64D tail. Alternatively, the association between ChAT and the KIF3A/KLP64D-tail could be strengthened by post-translational modifications. Indeed, an earlier study reported that recombinant DmKAP could pull-down endogenous ChAT along with the motor subunits at 400 mM KCl (30). Altogether, these results established that ChAT directly binds to the KLP64D tail. It also confirmed that, even though ectopically expressed, the soluble form of recombinant GFP::ChAT also binds to KLP64D tail *ex vivo*.

KLP64D tail is essential for GFP::ChAT recovery in the axons

To confirm the *in vitro* results, we tested the role of the KLP64D tail in GFP::ChAT-recovery in axons at 78 h AEL. The recovery was significantly lower than the

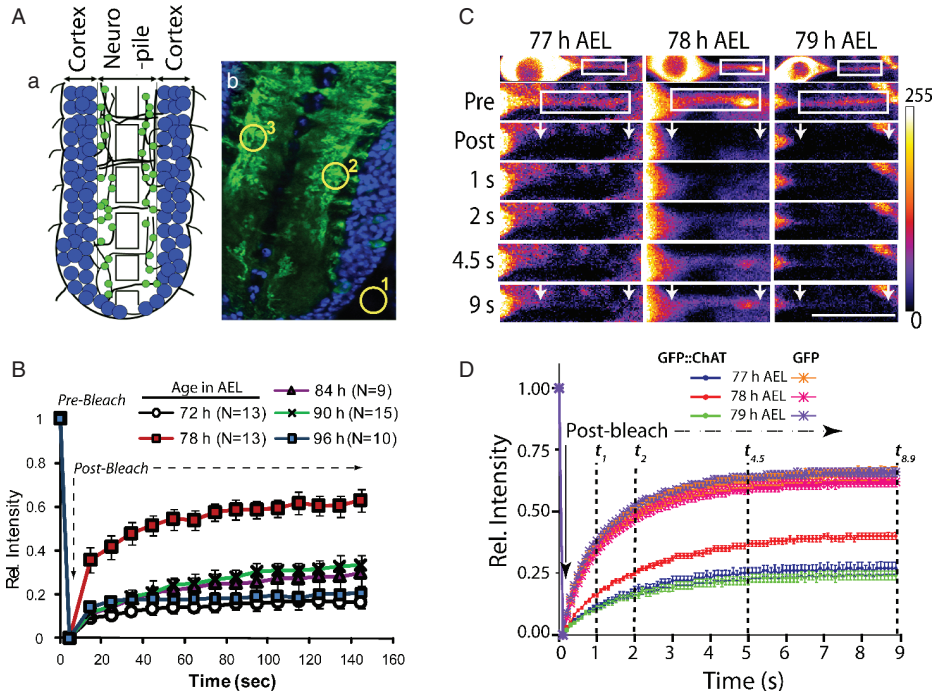

Figure 2: Fluorescence recovery after photobleaching (FRAP) of GFP::ChAT in the synapses and axons of larval ventral ganglia. A) Cellular organization (a), and GFP::ChAT localization (b) in the ventral ganglion (VG) of a third instar larva: (a) Interneurons, with their cell bodies (blue) in the cortex, extend the neurites and form synapses (green) in the neuropile region. b) The pattern is recapitulated in the DAPI-stained (blue) VG of *Cha*-GAL4>UAS-GFP::ChAT/+ larvae. DAPI marked the neuronal nuclei in the cortex while the GFP::ChAT (green) was mainly localized in the neuropile. Circles 1, 2 and 3 (diameter: 2.5 μm each) indicate positions of the background, photobleached and reference ROIs, respectively. B) GFP::ChAT FRAP in the neuropile of *Cha*-GAL4>UAS-GFP::ChAT VG at different stages of third instar larva. The RI changes are calculated as per the equation described in the *Methods*; N indicates the sample size; and the error bars indicate ±SE. C) GFP-ChAT FRAP in the axons at 77 h, 78 h and 79 h AEL (scale bar 10 μm, ROI: 10.4 × 1.15 μm, collected at 10 fps). The intensity changes are depicted in 8-bit pseudo color map as per the scale on the right margin. The top row contains images of the interneuron while the corresponding axon is shown in the subsequent panels. The photobleached ROI is shown as a white box in the first two rows and by arrows in the post-bleach and last frame (9 seconds) panels of the montages. D) The FRAP data obtained from the *Cha*-GAL4>UAS-eGFP/+ (GFP) and the *Cha*-GAL4>UAS-GFP::ChAT/+ (GFP::ChAT) VG, at 10 fps, are presented according to the normalized RI scale ($N \geq 15$). The GFP-FRAP profiles overlap with each other at all three larval stages, whereas the GFP::ChAT FRAP profile at 78 h AEL (red) is significantly higher than those obtained at 77 h (blue) and 79 h (green) AEL.

wild-type control in the homozygous *Klp64D* mutant larvae (Figure 4A,B), though the GFP FRAP profile, obtained from the VG of the mutant larvae was almost identical to that of the wild-type controls (Figure 4B). A similar result was obtained in the dorsal neuropile (Figure S3). This ruled out the possibility of the wild-type phenomenon being an over expression artifact. The expression of a full-length recombinant KLP64D protein in the *Klp64D* homozygous mutant backgrounds (***Rescue_1***) restored GFP::ChAT FRAP to wild-type levels (Figures 4A,B and S3). This showed that indeed KLP64D is required for GFP::ChAT flow in the axon. We also noticed a high level of GFP::ChAT fluorescence in the cell bodies, in ***Rescue_1*** VG (Figure 4A). We reasoned that only a part of the recombinant protein, because of its ectopic expression, would go into the functional kinesin-2 complex and transport ChAT in the axons. The remaining KLP64D::TEV-His could sequester GFP::ChAT and ChAT into immobile complexes in the cell body. Hence, we used this system to further study the role of KLP64D tail in GFP::ChAT FRAP. For this, we co-expressed a tailless recombinant transgene (*UAS-KLP64D(ΔT)::TEV-His*) in the cholinergic neurons along with GFP::ChAT in *Klp64D*^{k1} homozygous background (***Rescue_2***). As expected, the GFP::ChAT FRAP remained at the mutant level (***Rescue_2***, Figure 4B), indicating that the KLP64D tail plays a crucial role in ChAT transport in the axons.

To corroborate that the recombinant KLP64D(ΔT) forms a complex with the other kinesin-2 subunits in the tissue we purified the recombinant motor from the head extracts of control (**I**) and transgenic stocks expressing the KLP64D(ΔT)::TEV-His (**II**), and full-length KLP64D::TEV-His (**III**) using Ni-NTA beads (Figure 4C). The endogenous KLP68D and DmKAP co-purified with the recombinant KLP64D(ΔT)::TEV-His and KLP64D::TEV-His from stocks **II** and **III**, respectively. However, only full-length KLP64D::TEV-His could pull down the endogenous and recombinant GFP::ChAT (Figure 4C). This confirmed that KLP64D tail is essential for ChAT binding to kinesin-2

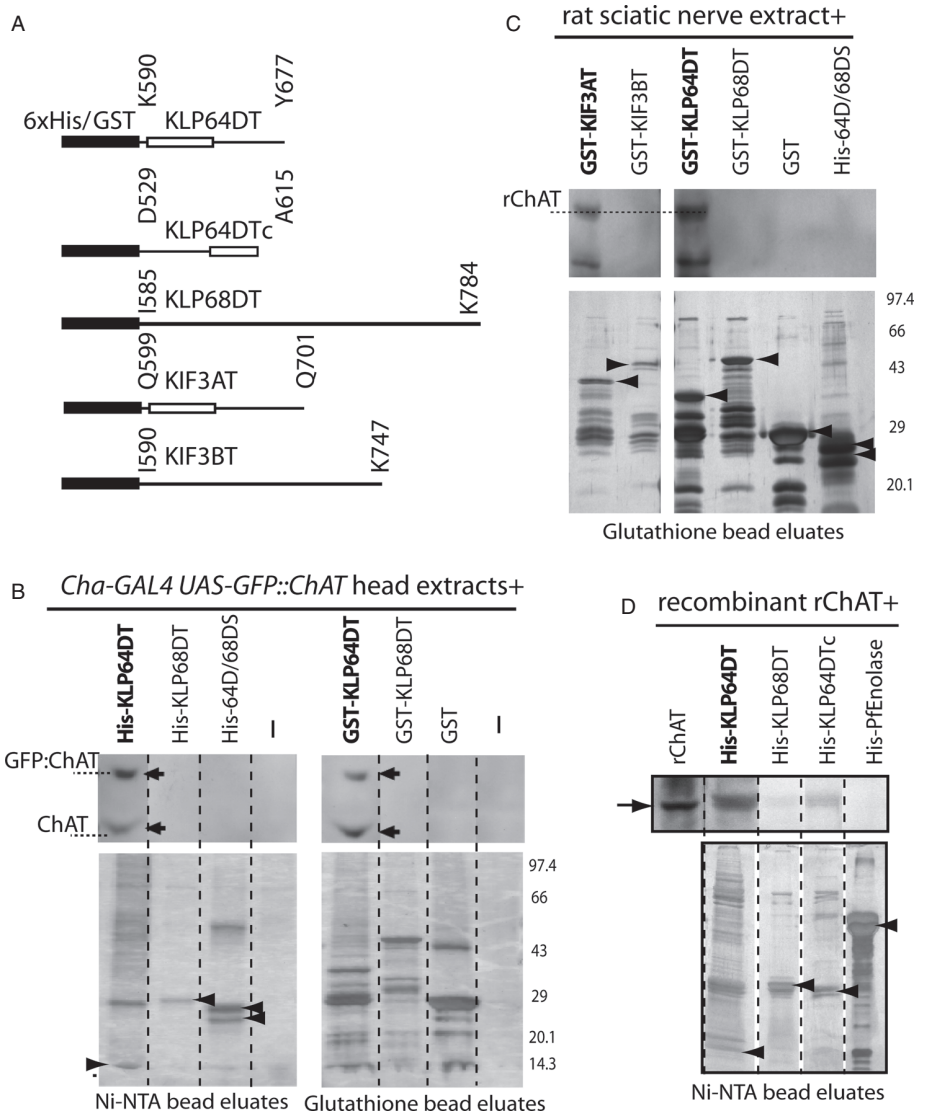

Figure 3: Soluble ChAT binds to the KLP64D tail *in vitro*. Recombinant KLP64D, KLP68D, KIF3A and KIF3B tail fragments (shown in the schematic in A) were separately mixed with 100 000 × ***g*** extracts of C*ha*-GAL4>UAS-GFP::ChAT fly heads (B), rat sciatic nerve (C) and *Escherichia coli* expressing recombinant rat ChAT (D). The mix was then affinity-purified using Ni-NTA or Glutathione Sepharose beads. Western blots of the bead eluates were stained with mAb4B1 (B) or anti-choactase (upper panels in C, D). Similar SDS-PAGE gels were also silver stained (lower panels). The open box in the schematic indicates the conserved region in KLP64D and KIF3A tails. Arrows indicate ChAT bands while arrowheads indicate the bait proteins of corresponding eluates in the silver-stained gels. Poly-His-tagged *Plasmodium falciparum* (*Pf*) enolase and the Glutathione *S*-Transferase (GST) were used as controls for non-specific binding.

in vivo, and further supported the FRAP data. In addition, we found that the KLP64D(ΔT)::GFP FRAP profile was identical to that of KLP64D::GFP in the VG axons in both wild-type and *Klp64D* homozygous mutant backgrounds (Figure S4), indicating that the deletion of the KLP64D tail does not restrict its movement in the axons. Therefore, the interaction between KLP64D tail and ChAT in the axon is essential for its transport to the synapse.

Furthermore, the recombinant GFP::tubulin84B, expressed in the cholinergic neurons of *Klp64D* homozygous mutants, localized normally in the axons (Figure S5), and GFP-FRAP in the *Klp64D* homozygous mutant background was similar to the wild-type level. These observations suggested that, unlike the kinesin-1 mutants (32,33), the axon channels were not blocked in the *Klp64D* mutant. Together with the previous data (24), these results established that ChAT transport by kinesin-2 in the axons requires an interaction with the KLP64D tail.

GFP::ChAT transport does not require KLP68D tail

The association between the motor subunits, KLP64D and KLP68D, is essential for kinesin-2 motor assembly (30). Therefore, the KLP68D deficit is expected to affect the ChAT transport as much as the one caused by the KLP64D loss. However, the affinity co-purification data suggest that process would not require the KLP68D tail. In order to prove this point, we measured the GFP::ChAT FRAP in the VG axons of *Klp68D*^{Bex2} homozygous mutant larvae at 78 h AEL. *Klp68D*^{Bex2} is a total loss-of-function allele, and as expected, the GFP::ChAT FRAP was reduced to the basal level in the mutant VG (Figure 5A,B). The expression of the full-length *KLP68D::YFP* transgene in the cholinergic neurons in the homozygous *Klp68D*^{Bex2} background rescued the defect to the wild-type level (Figure 5B). Finally, even though the expression of the KLP68DΔT::YFP in the homozygous *Klp68D*^{Bex2} background failed to rescue the recessive lethality, the GFP::ChAT FRAP was perfectly normal (Figure 5B). This

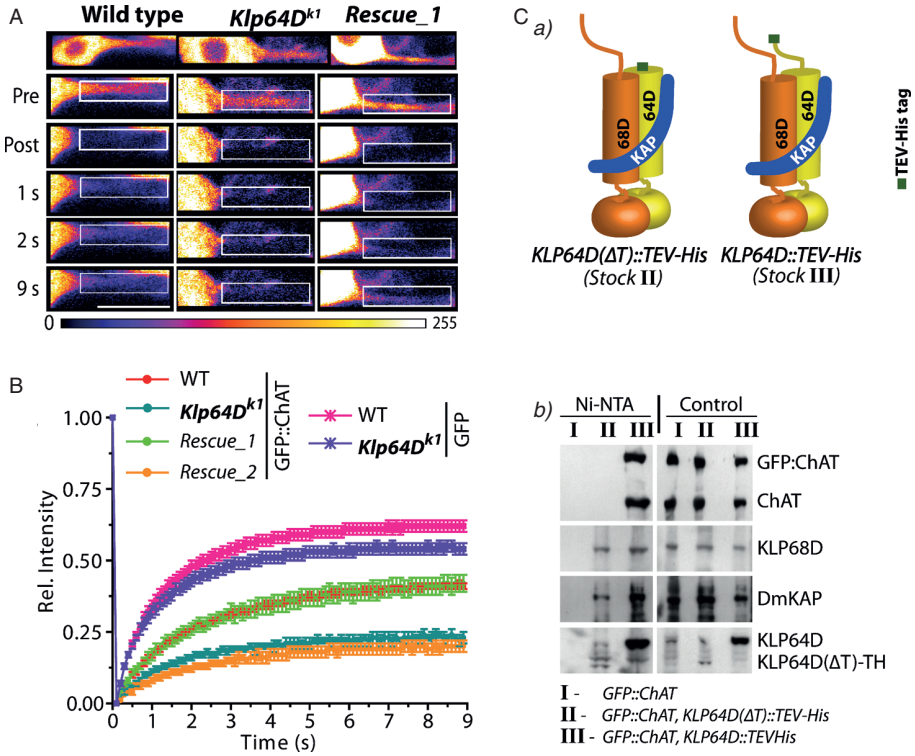

Figure 4: GFP::ChAT-FRAP at 78 h AEL requires the KLP64D tail. A) Time lapse images of GFP::ChAT-FRAP in the axons of the selected VG neuron from *Cha*-GAL4>UAS-GFP::ChAT/+ (wild-type), *Cha*-GAL4>UAS-GFP::ChAT/+; Klp64D^{k1} (*Klp64D^{k1}*mutants) and *Cha*-GAL4>UAS-GFP::ChAT/UAS-KLP64D::TEV-*His;* Klp64D^{k1} (***Rescue_1***) larvae. White boxes show the photo-bleached ROI in each panel (scale bar = 10 μm, ROI: 10.4 × 1.15 μm, obtained at 10 fps), and the time stamps at the left margin indicate the post-bleach interval. B) GFP::ChAT and GFP-FRAP profiles in the axons from wild-type and Klp64D^{k1}, *Cha*-GAL4>UAS-GFP::ChAT/UAS-KLP64D::TEV-*His;* Klp64D^{k1} (***Rescue_1***) and *Cha*-GAL4>UAS-GFP::ChAT/UAS-KLP64D*(T)*::TEV-*His;* Klp64D^{k1} (***Rescue_2***) VG. Error bars indicate ±SE, $N \geq 12$ for all samples, and Table S1 lists *p*-values indicating the significance of difference between the wild-type and mutant FRAP data. C) KLP64D tail is essential for kinesin-2 and ChAT association *in vivo*. a) Schematics illustrate kinesin-2 compositions in stocks **II** and **III**, containing the recombinant KLP64D(ΔT)::TEV-His and KLP64D::TEV-His, respectively. (b) Ni-NTA bead eluates from the head extracts of *Cha*-GAL4>UAS-GFP::ChAT/+ (**I**), *Cha*-GAL4>UAS-GFP::ChAT/UAS-KLP64D*(T)*::TEV-*His* (**II**), and *Cha*-GAL4>UAS-GFP::ChAT/UAS-KLP64D::TEV-*His* (**III**) stocks were western blotted and stained with mAbChAT, anti-KLP68D, mAbDmKAP and mAbKLP64D. Positions of KLP68D, DmKAP, KLP64DT::TEV-His (KLP64DT-TH) and KLP64D (same for KLP64D::TEV-His), along with ChAT and GFP::ChAT are indicated on the right margins.

established that the KLP68D tail is redundant for ChAT transport although it is essential for the other kinesin-2 functions.

Interaction with the Klp64D-tail facilitates ChAT entry into the axon initial segment

The presence of a cytoplasmic filter in the axon initial segment (AIS) has been described, which prevents the diffusive entry of larger molecules, such as fluorescein-dextran (>70 kDa), into the axons (34). This could potentially regulate ChAT entry into the axon. The AIS was manually specified as the region where the diameter of the axon is 1/10th of the minor axis of the ellipsoid cell body in the larval VG (arrows, Figure 6A). FRAP analysis in 10.4 × 1.15 μm ROIs, covering parts of the cell body and axon around the AIS, showed that the GFP::ChAT recovery was visibly low in the AIS as compared to the cell body, and was almost abolished in the homozygous *Klp64D* mutant neuron (Figure 6A). Simultaneous FRAP analyses, performed in two smaller ROIs (5.2 × 1.15 μm each) in the cell body and around the AIS to quantify the phenomenon, indicated that the recovery in the cell body-ROI was comparable in the wild-type and KLP64D(ΔT) (***Rescue_2***) backgrounds. However, it was significantly lower in the AIS-ROI in the ***Rescue_2*** stocks (Figure 6B,C), suggesting that the ChAT movement into the AIS required KLP64D-tail.

However, the FRAP analyses in different larval stages also showed that a significant part (approximately 50%) of the GFP::ChAT mobility in the axon was kinesin-2 independent. Approximately 20% of GFP::ChAT recovery occurred within 9 seconds, in both the homozygous *Klp64D* and *Klp68D* mutants, in the AIS and axons at 78 h AEL. This could be contributed by retrograde flow and motor-independent processes. The detector shot noise could also contribute to a part of the baseline recovery.

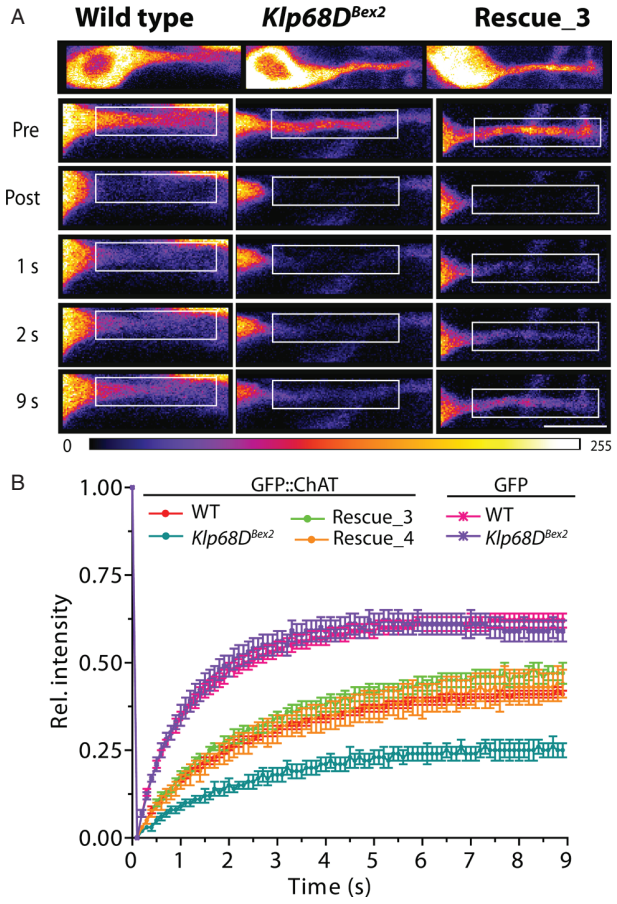

Figure 5: GFP::ChAT-FRAP at 78 h AEL in homozygous KLP68D mutant and rescued stocks. A) Time lapse images of GFP::ChAT-FRAP in the axons of the selected VG neuron from *Cha*-GAL4>UAS-GFP::ChAT/+ (wild-type), *Cha*-GAL4>UAS-GFP::ChAT/+; Klp68D^{Bex2} (Klp68D^{Bex2}) and *Cha*-GAL4>UAS-GFP::ChAT/UAS-KLP68D::YFP; Klp68D^{Bex2} (***Rescue_3***) larvae. White boxes show the photo-bleached ROI in each panel (ROI: 10.4 × 1.15 µm, obtained at 10 fps), and the time stamps at the right panel indicate the post-bleach intervals. Scale bar = 10 µm. B) GFP::ChAT and GFP-FRAP profiles in the axons from wild-type and Klp68D^{Bex2}, *Cha*-GAL4>UAS-GFP::ChAT/UAS-KLP68D::YFP; Klp68D^{Bex2} (***Rescue_3***) and *Cha*-GAL4>UAS-GFP::ChAT/UAS-KLP68D*(T)*::YFP; Klp68D^{Bex2} (***Rescue_4***) VG. Error bars indicate ±SE, $N \geq 5$ for all samples.

Additionally, an indirect role of kinesin-1 or some other motors in the process cannot be ruled out, although the affinity co-purification data did not indicate ChAT association with kinesin-1 *in vitro*.

GFP::ChAT flow in axons has an anterograde bias

The dynamic OTSU thresholding of an image (see *Materials and Methods*) can remove the shot noise. Kymographs, generated from the thresholded movies (Figure 7A), revealed that GFP::ChAT recovered with an anterograde bias, and in a manner, similar to KLP64D::GFP (Figure 7B). This was absent in the kinesin-2 mutants. In contrast, GFP recovery in the axon was rapid and bidirectional (Figure 7B). The recovery fronts were initially linear and then became hyperbolic. A line fit to the initial phase showed that both GFP::ChAT and KLP64D::GFP fronts move at similar rates (Table 1). To further determine the direction of the net flow, we divided the bleached ROI into three equal compartments and analyzed the recovery by integrating the fluorescence in each one of them (Figure 7C). This showed that GFP::ChAT recovers at a significantly faster rate in the anterograde ROI (AR) than in the retrograde ROI (RR), (Figure 7C). Although the initial GFP recovery was marginally faster in the AR than that in the RR, it became equal within 4 seconds. Thus, relatively higher anterograde flow in the axons, at 78 h AEL, could account for the ultimate ChAT enrichment in the presynaptic compartment. Interestingly, we could not identify any particulate form of movement during GFP::ChAT recovery. Calibration of the confocal system used indicated the minimum detection limit at 4–10 GFP fluorophores/voxel. This ruled out the existence of large, transient GFP::ChAT aggregates. Hence, monomeric or small oligomeric complexes of GFP::ChAT is likely to constitute the overall bulk flow of the protein toward the synapse. This is a unique phenomenon for a kinesin 2-based intracellular transport.

Kinesin-2 is a plus-end directed MT-based motor, and it transports axonal cargoes toward the synapse. The clear anterograde bias in the GFP::ChAT recovery and its dependence on the kinesin-2 tail suggest that the endogenous ChAT flow is also aided by the motor in axons. The lack of any particulate movement during the recovery indicates that the mobile fraction of GFP::ChAT/ChAT is not organized into large aggregates. The GFP::ChAT recovery fronts were not sharply defined, and the regression analysis showed that the average front velocities slow down with time (Table 1). Together this evidence suggested that a significant part of the ChAT movements in the axon would be diffusive. The recombinant tail pull-down results suggested that the affinity between ChAT and kinesin-2 tail is low *in vitro*, and thus, the binding could be disrupted because of viscous drag in the cytoplasm (35). Moreover, individual kinesin-2 is a motor with low processivity (36), which could further affect the progression of GFP::ChAT front. Together, all these could generate the diffusion-like flow of ChAT in axons.

ChAT obtained from fly head is not polymorphic

Drosophila head extracts contain both the hydrophilic and amphiphilic forms of ChAT (37). The soluble form obtained from the rat brain binds to the plasma membrane of cholinergic synaptosomes (38). These two studies also showed that ChAT does not localize to synaptic vesicles. The form in which ChAT would be transported in the axons was, however, unclear. We found that a majority of ChAT was present in the soluble fractions of *Drosophila* head extracts, and the membrane associated form became soluble in PMEE containing 1% Triton X-100 (Figure 8A-a). Additionally, most of the GFP::ChAT found in the neuronal

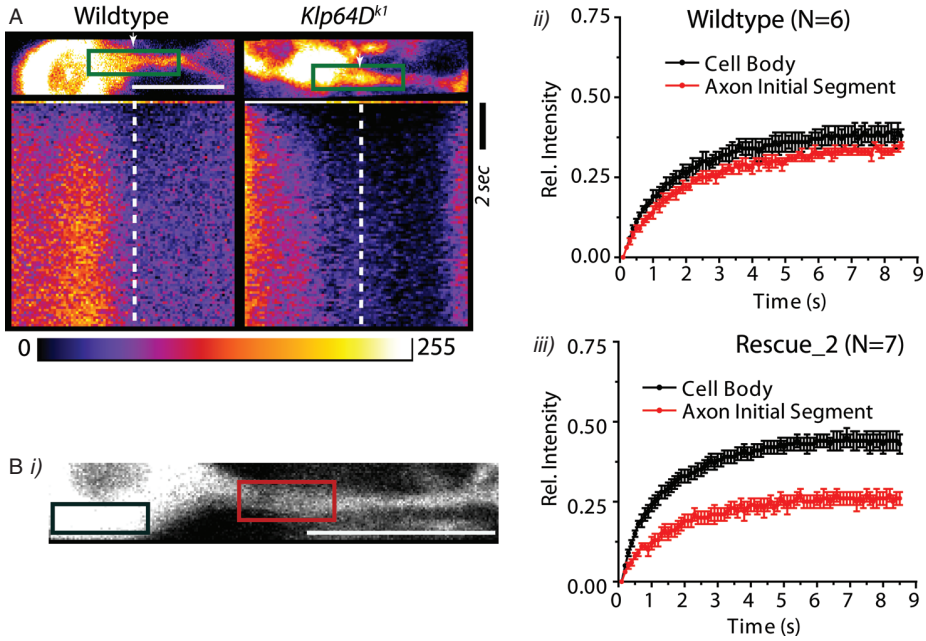

Figure 6: KLP64D tail is required for axonal entry of GFP::ChAT at 78 h AEL. A) The boxes in the upper panels indicate photobleach ROIs in the neurons obtained from *Cha*-GAL4>UAS-GFP::ChAT/+ (wild-type) and *Cha*-GAL4>UAS-GFP::ChAT/+; Klp64D^{k1} VGs. Kymographs in the lower panels depict GFP::ChAT FRAP at the transition region between cell body and axon. The axon initial segment (AIS) is marked by arrows and dotted lines in the respective panels. The gray scale intensity levels are presented in a 0–255 heat map scale as indicated in the bottom panel. ROI: 10.4 × 1.15 μm, obtained at 10 fps. B) GFP::ChAT FRAP in the cell body (black box, i) and axon initial segment (red box, i). Quantification of GFP::ChAT recoveries in these two ROIs in *Cha*-GAL4>UAS-GFP::ChAT/+ (wild-type, ii) and *Cha*-GAL4>UAS-GFP::ChAT/UAS-KLP64D*(T)*::TEV-*His*;Klp64D^{k1} (Rescue_2, iii) backgrounds. Error bars indicate ±S.E. while *N* denotes the sample size. ROI: 5.2 × 1.15 μm; scale bar for (A) and (B-i) = 10 μm.

cell body and VG axons got extracted with 0.3% triton-X-100 after fixation (Figure 8A-b). Purified kinesin-2 complex from sea urchin embryos sediment at 8–9˜S˜(39), and monomeric ChAT, according to its globular size (22), is expected to sediment a little ahead of albumin (4.6 S) on a density gradient. Both the 75 kDa ChAT and the kinesin-2 subunits, KLP68D and DmKAP, were concentrated in fractions 9–11 on a sucrose density gradient, a little ahead of the albumin (Figure 8B-a). A similar co-migration was obtained using extracts from mouse motor axons earlier (29). A considerable amount of the detergent-extracted ChAT, however, sedimented in low-density fractions independent of kinesin-2 (Figure 8B-b), and the spread was continuous. The presynaptic ChAT in the adult brain, associated with synaptic plasma membrane, is solubilized with triton-X100, and this could cause poly-dispersive migration on the gradient.

The ChAT and kinesin-2 bands shifted toward the lighter fractions at 400 mM KCl (Figure 8B-c). Kinesin-2 acquires an extended conformation at high KCl (39), and many of the motor–cargo complexes dissociate at high salt. Together these two phenomena could cause the upward shifts of KLP68D and DmKAP bands. However, the concomitant shift of ChAT bands was unexpected. We have earlier shown that though endogenous ChAT co-precipitates with kinesin-2 motor subunits at 400 mM KCl, only a small fraction of soluble ChAT was co-sedimented with MT (30). This could account for the shift of a part of the ChAT bands. Moreover, ChAT is a globular protein, which is unlikely to have extended conformations. However, a recent report showed that ChAT could associate with KAP3 along with SOD1 in mouse axons (29). Hence, in addition to the kinesin-2 associated forms, the soluble ChAT may also associate with several other proteins or it may form oligomers that could dissociate at high ionic strength, causing a shift in the ChAT bands on sucrose density gradient. Overall, the size of the ChAT and the kinesin-2 complex is smaller than the axonal CamKIIa, which sediments at unusually high sucrose density (21).

Discussion

Slow axonal transport is a multivariate phenomenon where different types of soluble proteins move bi-directionally, *en bloc* at a variety of different rates in the axon. In fact, the role of the motor protein was once proposed to be minimal in this process (1). Indeed, a part of the hypothesis is indicated to be untrue by a host of recent reports (11,15,17,18,20,21). In addition, stochastic simulation indicated that 'stop and go' movements of large soluble aggregates could give rise to the net slow rate of the axonal transport of soluble proteins

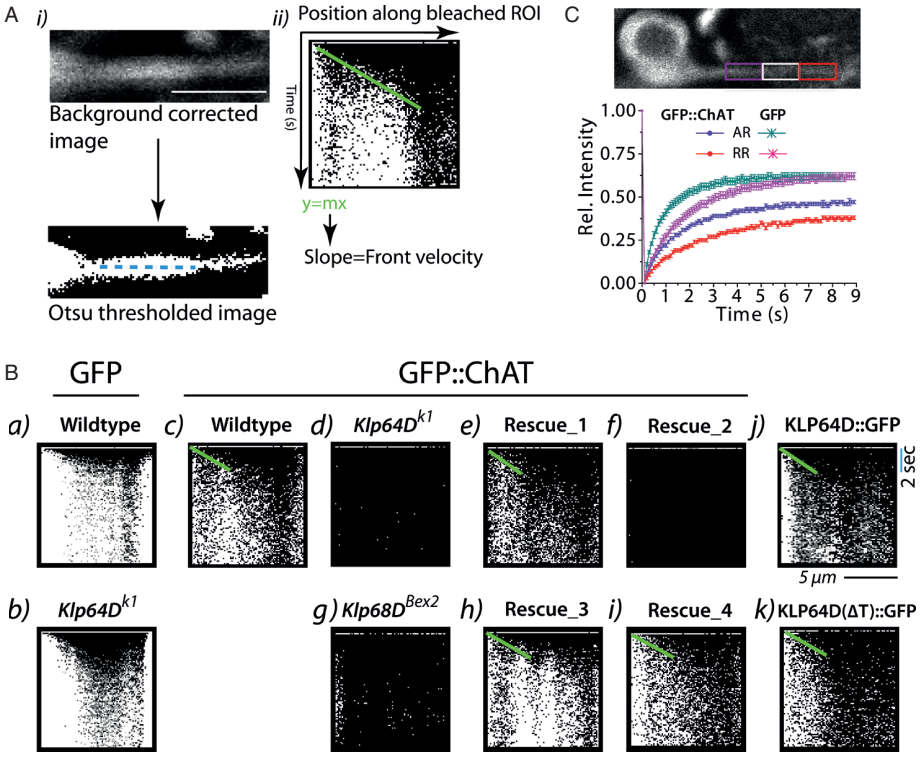

Figure 7: The non-particulate flow of GFP::ChAT in the axons shows an anterograde bias. A) Otsu thresholding of the axon to determine the movement of front of GFP::ChAT. The 8-bit, background corrected image is dynamically thresholded, by using the Otsu thresholding plugin of ImageJ, to obtain a binary image (i). A kymograph (ii) is generated for a 90 × 5 pixels line (broken blue line, i) marked on the thresholded image, depicting the fluorescence recovery pattern along the photobleached region of the axon (*x*-axis, length; *y*-axis, time). A linear fit to this distribution provides the position of the front during recovery (green line). The slope of this line (m), obtained from the equation, provides the estimated front velocity. B) Kymographs depicting the axonal recovery patterns of GFP (a and b), GFP::ChAT (c–i), KLP64D::GFP (*j*) and KLP64D (T)::GFP (k) in wild-type controls (a, c, j, k), Klp64D^{k1} homozygous (b, d) and Klp68D^{Bex2} homozygous (g) mutant VG. Kymographs in (e) and (f) were obtained from the C*ha*-GAL4>UAS-GFP::ChAT/UAS-KLP64D*(ΔT)*::TEV-*His;* Klp64D^{k1} (Rescue_1) and *Cha*-GAL4>UAS-GFP::ChAT/UAS-KLP64D*(ΔT)*::TEV-*His;* Klp64D^{k1} (Rescue_2), while those in figures (h) and (i) were from the C*ha*-GAL4>UAS-GFP::ChAT/UAS-KLP68D::YFP*;* Klp68D^{Bex2} (Rescue_3) and C*ha*-GAL4>UAS-GFP::ChAT/UAS-KLP68D*(ΔT)*::YFP*;* Klp68D^{Bex2} (Rescue_4), respectively. C) GFP and GFP::ChAT-FRAP in the anterograde (AR) and retrograde (RR) ROIs. Inset, magenta and red boxes mark the AR and RR in a GFP::ChAT expressing neuron. The green lines indicate liner fit of the recovery front in the first 2 seconds. Total ROI length: 10.4 µm and observation time: 8.9 seconds after photobleach. Scale bar in (A) and (C) = 10 µm.

(16,19). The mode of bulk movement was elegantly demonstrated by monitoring synapsin-1 and CamKIIa transport in axons recently (21). Though kinesin-1 is implicated in all these movements, association between the motor and cargoes has not been demonstrated. In addition, most of the reports so far, indicate that the motor–cargo interactions during axonal transport occur through adaptors or scaffolding proteins, which link the motors to different cargoes (40,41). This is proposed to maintain the specificity, as well as divergence, in the transport process propelled by a motor protein. The results presented here point toward another alternative, i.e. transport of individual soluble proteins through a direct interaction with the kinesin-2 motor, which is globally regulated in brief, dispersed time domains. The above data also show that even though carried by the kinesin-2 motor, the mechanism of ChAT transport in axons is quite distinct from that of many other SCb proteins (11,17,20,21).

We observed that during the scheduled period, the GFP::ChAT recovery rates matched that of the KLP64D::GFP (Table 1), which suggests that the GFP::ChAT flow occurs at the average kinesin-2 speed in axons. However, it lacked particulate features and the recovery front movement progressively slowed with time. Preliminary simulations suggest that a combination of motor-driven movement and diffusion in the axons could produce a GFP::ChAT front similar to the one observed in the experimental kymographs (Jana S., Vinod Kumar and Menon G., personal communication). This would be distinct from the persistent, long run of a motor–cargo complex in the axon. Interestingly, the simulation also predicted that the GFP recovery would be motor function independent. Therefore, we propose that kinesin-2 is likely to guide the bulk flow of ChAT in axons through weak, occasional association with the KLP64D/KIF3A tail as it moves toward the synapse. A similar mechanism

Table 1: Front velocity calculations from the FRAP Kymographs.

Label	Genotype	Front velocity (μm/second)	
		After 1 second	After 2 seconds
a)	*Cha-GAL4>UAS-GFP/+*	1.44 ± 0.2	0.96 ± 0.2
b)	*Cha-GAL4>UAS-GFP/+; Klp64D^{k1}-*	1.11 ± 0.2	0.61 ± 0.2
c)	*Cha-GAL4>UAS-GFP::ChAT/+*	0.97 ± 0.4	0.62 ± 0.3
d)	*Cha-GAL4>UAS-GFP::ChAT/+; Klp64D^{k1}*	No recovery	
e)	*Cha-GAL4>UAS-GFP::ChAT/UAS-KLP64D::TEV-His; Klp64D^{k1}* ***(Rescue_1)***	1.2 ± 0.2	0.78 ± 0.1
f)	*Cha-GAL4>UAS-GFP::ChAT/UAS-KLP64D(ΔT)::TEV-His; Klp64D^{k1}* ***(Rescue_2)***	No recovery	
g)	*Cha-GAL4>UAS-GFP::ChAT/+; Klp68D^{Bex2}*	No recovery	
h)	*Cha-GAL4>UAS-GFP::ChAT/UAS-KLP68D::YFP; Klp68D^{Bex2}* ***(Rescue_3)***	1.14 ± 0.12	0.99 ±0.15
i)	*Cha-GAL4>UAS-GFP::ChAT/UAS-KLP68D(ΔT)::YFP; Klp68D^{Bex2}* ***(Rescue_4)***	1.41 ± 0.31	0.98 ± 0.35
j)	*Cha-GAL4>UAS-KLP64D::GFP/+*	1.01 ± 0.67	0.59 ± 0.22
k)	*Cha-GAL4>UAS-KLP64D(ΔT)::GFP/+*	1.33 ± 0.65	0.73 ± 0.35

Representative kymographs are shown in Figure 7B, and the velocities are calculated as the slopes of the regression fit line as shown in figure. Sample size: $N \geq 10$ for genotypes a–f, j, and k; and $N \geq 5$ for genotypes g–i.

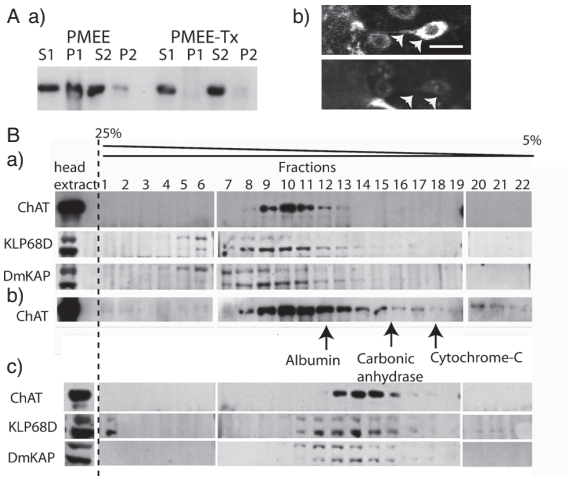

Figure 8: Free and motor-bound forms of ChAT have comparable densities. A) Biochemical characterization of endogenous ChAT and GFP::ChAT. a) Western blots of fly head extracts, in PMEE, and PMEE containing 1% triton-X-100 (PMEE-Tx), stained with mAb4b1. S1 and P1 – supernatant and pellet fractions, respectively, obtained after a 17 000 × ***g***, 30 min centrifugation of the homogenate. S2 and P2 – supernatant and pellet fractions, respectively, obtained after a 100 000 × ***g***, 1 h centrifugation of the S1 fraction. b) Interneurons from live (upper panel) and fixed (lower panel) preparations of the *Cha*-GAL4>UAS-GFP::ChAT/+ VG. Scale bar = 10 μm. B) Sucrose density sedimentation of the S2 fractions of the fly head extracts in PMEE (a), PMEE-Tx (b) and in PMEE containing 400 mM KCl (c). Western blots of the fractions are stained with mAb4B1 (ChAT), anti-KLP68D and mAbDmKAP.

is proposed to maintain the bulk flow of CamKIIa and synapsin-1 by kinesin-1 (21).

The other intriguing observation made in this study is the significantly low levels of the GFP::ChAT recovery outside the 77–79 h AEL window. Although both GFP::ChAT and KLP64D::GFP were expressed in the cholinergic neurons using the same *Cha-GAL4* driver, KLP64D::GFP recovered constitutively throughout the larval period (Figure S5). This implies that the interaction between KLP64D tail and ChAT is globally regulated, and this could restrict the episodes of its transport in the axons, resulting in an overall slow rate of accumulation as measured at the sciatic nerve ligatures earlier (23). This is quite different from the episodic fast transport of large soluble aggregate/oligomer (15,18,42) and filaments (12,13), as well as the dynamic switching of kinesin-1 motor between the slow and fast modes of transport by Hsc71 (42). This is a unique realization of this study, which was not reported for the other SCb cargoes. We described the slow axonal transport of a soluble protein in real time within an intact network, and established a new model to investigate axonal transport regulation in a neuron under a native context. Most importantly, it would allow us to probe the relationship between the nervous system development and slow axonal transport. In addition, one could also use this paradigm to test how modulation of neuronal physiology affects axonal transport of soluble and membrane bound presynaptic cargoes.

The FRAP analysis suggests that even though both ChAT and KLP64D is distributed all through the cell body and axon, the interaction between these two is spatially regulated. It occurs at the AIS, which perhaps helps to push the molecule into the axon. The AIS is proposed to contain a molecular filter (34), but little is known about the mechanism of its action. Establishing the two-component system involving KLP64D tail and ChAT opened up the possibility of identifying the molecular regulation of affinity between these two proteins *in vivo*. Therefore, to understand further, the regulation of the ChAT and kinesin-2 interaction *in vivo*, we will now have to identify the cellular kinematics of this process at higher sensitivity and spatiotemporal resolution. Asymmetric distribution of proteins results in compartmentalization of cellular function, and is essential for directed transfer of information within a cell. The functional diversity of different cells also arises from the intrinsic asymmetry

in protein localization (43–45). It is already established that such asymmetric enrichment of membrane-bound proteins occurs due to selected targeting to the plasma membrane or organelles through the concerted actions of small GTPases and motors (46). Such differential localization is also observed even for small soluble proteins that are free to diffuse. However, the creation and maintenance of asymmetric distribution of easily diffusible soluble proteins are intriguing. Therefore, the results presented here could also provide clues about the mechanism underlying the asymmetric enrichment of other soluble proteins *in vivo*.

Materials and Methods

Preparation of transgenic fly stocks and Drosophila culture

Full-length ChAT with an N-terminal GFP was cloned into the pUAST vector between the *Not*I and *Xba*I sites and a transgenic *pUAS-GFP::ChAT* fly stock was obtained using standard procedures (47,48). All other stocks used in this study are listed in Table S3. All fly stocks were reared in 12-h light–dark cycles at 25°C on standard corn meal agar medium supplemented with yeast.

Immunoprecipitation and Ni-NTA/GST co-purifications using fly head extract

Fly heads were decapitated and homogenized in (2 μL/head) HEPES buffer (20 mM HEPES, 100 mM NaCl, 40 mM KCl, 5 mM $MgSO_4$, 5 mM EGTA, 1 mM DTT, protease inhibitor cocktail (Roche Diagnostics, pH = 7.4) using a Teflon pestle. After clearing the tissue debris by centrifuging at 40 000 × ***g*** for 45 min, the crude extract was ultra-centrifuged at 100 000 × ***g*** for 1 h, at 4°C, to obtain a supernatant/fly head extract, and pellet containing soluble and membrane-bound proteins, respectively.

For Ni-NTA/GST co-purifications, 100 μL of supernatant was incubated for 1 h at 4°C with appropriate volumes of His- or GST-tagged bait protein (final concentration = 4 μM). This was followed by incubation with 300 μL of equilibrated Ni-NTA agarose/Glutathione-sepharose beads. For analysis of ChAT: kinesin-2 interactions, *in vivo*, 100 μL of Ni-NTA/Sepharose-G beads were directly incubated with appropriate fly head extracts for 1 h at 23°C. After five washes with 10× bead volume of HEPES buffer, the beads were boiled in SDS sample buffer and analyzed by SDS-PAGE and western blotting.

Bacterial cells expressing the bait proteins were suspended in TMN (20 mM Tris–Cl, 5 mM $MgCl_2$, 300 mM NaCl, 1 mM DTT, 20 mM Imidazole, pH 7.4) and lysed by sonication after a 1 unit/mL lysozyme treatment for 30 min. After centrifugation at 17 000 × ***g*** in 4°C for an hour, the supernatants were mixed together in following proportions: 10 mL of rChAT extract was incubated with 25 mL of the extract containing the bait proteins, for 90 min at 4°C. The mixture was then incubated with 2 mL of equilibrated bead slurry on a rocker for 1 h at 4°C. The mixture was allowed to stand for 30 min after transferring to a column, and then the beads were washed 10 times with 1 mL TMN containing 50 mM imidazole/wash. The bound proteins were then eluted with 1 mL TMN containing 250 mM imidazole.

SDS-PAGE and western blotting

The supernatant fractions, thus obtained, were resolved by SDS-PAGE and transferred onto a PVDF membrane (Hybond-P Amersham) in 1× Towbin's buffer. After an overnight blocking in 5% milk, the blots were probed using appropriate primary and secondary antibodies (Table S2). The blots were then developed using ECL™ chemiluminescence kit (GE Healthcare Ltd.)

Fluorescence recovery after photobleaching (FRAP) assay

Ventral ganglia (VG) from appropriately aged third instar larvae were dissected in *Drosophila* physiological saline (128 mM NaCl, 2 mM KCl, 4 mM $MgCl_2$, 1.8 mM $CaCl_2$, 35.5 mM sucrose, 5 mM HEPES, pH = 7.4), mounted on a glass-bottom Petri dish and imaged using an Olympus FV1000SPD laser scanning confocal microscope.

For the FRAP assay in dorsal neuropile, samples were observed in 512*512 pixel format using 60× 1.2 NA water objective lens with an additional 1.4× zoom. A circular ROI of 25-pixel diameter (approximately 20 μm^2) was defined (ROI_3, Figure 1A) and photobleached up to 40–80% of initial intensity using 0.6 mW 488 nm laser line. Subsequent recovery was monitored at the rate of 1-frame every 5 seconds using 0.02–0.03 mW laser power. Two 25-pixel circular ROIs were selected from an area outside the sample (ROI_1) for background, and from within the corresponding segment of the VG (ROI_2) for acquisition bleaching corrections, respectively.

FRAP assay in single axons was performed using a 60×, 1.42 NA oil objective and additional optical zoom of 3.6×. Inter-neurons, whose axons were clearly visible, were chosen for FRAP measurements from the ventrocentral sections of the VG. A 90 × 10 pixel (10.4 × 1.15 μm) photobleached ROI was defined along the axon. To compare GFP::ChAT mobility in the AIS and cell body regions, two separate ROIs (45 × 10 pixels each) were specified in appropriate locations (Figure 6B-i). One frame was acquired before bleaching (pre-bleach frame) using the 37.8 μW of laser power (488 nm). For photobleaching, the laser power was stepped up to 900 μW, and the total ROI was scanned 10 times (at 8 μseconds/pixel). FRAP was monitored in the subsequent 88 frames, recorded at the same laser power as the pre-bleach frame, resulting in 9 seconds of observation. The ROI frame was scanned in 100 milliseconds (at 4 μseconds/pixel), thereby, giving a net 10 Hz frame rate. At 0.6 μm/second speed, kinesin-2 is estimated to spend approximately 0.2 second in a pixel.

Data analysis

The raw fluorescence data were exported to Microsoft excel spread sheet for further quantification. Relative intensity (RI) was calculated using the following equation:

$$\mathrm{RI}\ (t) = F_{(t)}/F_{(i)1}$$

where $F_{(t)}$ is the fluorescence intensity at time-point t, and $F_{(i)}$ is the pre-bleach intensity. This data was corrected for the fluorescence change due to ROI_{Aq} and background fluorescence was subtracted to generate a plot of corrected relative intensity (cRI) versus time using the following equation:

$$\mathrm{cRI}_{(t)} = \left[F_{(t)} - F_{(\mathrm{Bk})t}\right] \Big/ \left[F_{(i)} - F_{(\mathrm{Bk})i}\right] \times \left[F_{(i)\mathrm{Aq}} - F_{(\mathrm{Bk})i}\right] \Big/ \left[F_{(t)\mathrm{Aq}} - F_{(\mathrm{Bk})t}\right]$$

where $F_{(i)\mathrm{Aq}}$ is the fluorescence intensity of ROI_{Aq} before bleaching, and $F_{(t)\mathrm{Aq}}$ is the fluorescence intensity of ROI_{Aq} at time-point t. The data were further plotted, as the fraction of recovery (FR) versus time to normalize the data using the following equation:

$$\mathrm{FR}\,(t) = \mathrm{cRI}_{(t)} - \mathrm{cRI}_{(\mathrm{min})} / \mathrm{cRI}_{(i)} - \mathrm{cRI}_{(\mathrm{min})}$$

where $\mathrm{cRI}_{(t)}$ is the corrected relative intensity at time t, $\mathrm{cRI}_{(i)}$ is the corrected pre-bleach intensity and $\mathrm{cRI}_{(\mathrm{min})}$ is corrected bleach intensity. The RI values of each post-bleach time-point, averaged across multiple movies, were plotted against time. The error bars indicate ±SE.

All representative images and movies were processed in the ImageJ® ver. 1.42 (National Institute of Health) and Adobe Photoshop CS2 (Adobe systems). The final images are represented in pseudocolor using 'Fire' LUT in ImageJ®.

Front velocity analysis

Background-corrected 16-bit raw images were converted into 8-bit images and converted to a binary (black/white) form by using the OTSU thresholding plugin of ImageJ® (http://rsbweb.nih.gov/ij/plugins/otsu-thresholding.html). A 90 × 5-pixel line was specified at the photobleached region of the axon. Kymographs were generated along this line. Co-ordinates of the white pixels on the kymograph were obtained and plotted using the Origin® Graph plotting software. A linear regression curve was fitted to this time-displacement plot keeping the *y*-intercept as zero. The slope of this line was used as a measure of the front velocity.

GFP::ChAT and GFP diffusion calculations

The GFP and GFP::ChAT diffusion coefficients in the cytoplasm were estimated by using the Stokes–Einstein equation:

$$D = k_B T / 6\pi\eta r$$

where k_B is the Boltzmann's constant (1.38×10^{-23} JK^{-1}); T is the absolute temperature (296 K); η is the viscosity of cytoplasm (3 centipoise or 3×10^{-3} Pa.second); r is the hydrodynamic radius ($r_{GFP::ChAT} = 5.79$ nm; $r_{GFP} = 2.4$ nm).

Acknowledgments

We thank Prof. L. S. B. Goldstein (UCSD) for unconditional support and generosity, Dr. K. Schimmelpfeng for help in making the GFP::ChAT construct, Vikash Singh for making the *pUAS-GFP::ChAT* stock and Akanksha Jain for the *Klp68D^{Bex2}/TM6B* stocks, respectively. This work is supported by TIFR intramural fund, and in part, by the FIRCA grant (NIH Grant 1 RO3 TWO5784) to K. R.

Supporting Information

Additional Supporting Information may be found in the online version of this article:

Figure S1: GFP and GFP::ChAT recovery in the neuropile region of VG of third instar larvae. A) FRAP recovery montage of GFP (a) at 78hAEL and of GFP::ChAT (b) at various stages of third instar larvae. A 25 μm circular ROI in the dorsal neuropile was photobleached to 40% of original intensity and the then images using the confocal laser scanning microscope at every 10 seconds. The quantification of recovery of GFP::ChAT is presented in Figure 1B of the main text. B) GFP-FRAP plot at early, middle and late stages of third instar. While GFP recovery was constitutive, the recovery of GFP::ChAT was observed specifically at 78hAEL.

Figure S2: Preliminary analysis of GFP::ChAT FRAP in the axon at early, middle and late third instar. A) Montage showing FRAP of GFP::ChAT in VG interneurons at 72 h (early), 78 h (middle) and 96 h (late) AEL. Arrows mark the start and end of the 5 μm ROI that was bleached for 3 seconds, and subsequently, the recovery was monitored at 1 frame every 5 seconds in a total recording of 120 seconds. B) Quantification of FRAP shown in (A). GFP::ChAT showed a selective recovery in the axons at 78hAEL, concomitant with the recovery in the neuropile at the same time period of development.

Figure S3: FRAP of GFP::ChAT in the dorsal neuropile in *Klp64D^{k1}* mutants. A) Recovery of GFP::ChAT in the neuropile in *Klp64D^{k1}* mutant VG (a), rescued with genomic (UAS-KLP64D) (b) and TEV-His tagged (UAS-KLP64D::TEV-His) transgene of KLP64D (c). The FRAP of GFP in Klp64D^{k1} mutants (d). B) Quantification of GFP::ChAT recovery in *Klp64D^{k1}* mutants at 72, 78, 84, 90 and 96 h AEL and rescue at 78hAEL by various transgenes of KLP64D. C) Quantification of GFP-FRAP in wild-type and *Klp64D^{k1}* mutant VG at 78hAEL. The flux of GFP::ChAT in the neuropile requires active transport by kinesin-2 while that of GFP is diffusive which corroborates well with previous results (24).

Figure S4: KLP64D::GFP and KLP64D(ΔT)::GFP Recovery profiles. A) Preliminary analysis of the FRAP profiles of KLP64D::GFP in axons of early, middle and late third instar VG, shown on an 8 bit (0-255) pseudocolor scale. A 4.5 μm long ROI (green arrowheads) in the axon was bleached, and recovery was monitored subsequently at 1 frame/10 seconds in a total recording of 150 seconds. B) Spatiotemporally resolved recovery of GFP-tagged full-length (KLP64D::GFP) and tail-less (KLP64D (ΔT)::GFP) KLP64D in VG axons at 78 h AEL. A 10.2 × 5.5 μm ROI (green arrowheads) was photobleached for 1 second, and subsequent recovery monitored up to 18 seonds. The accompanying graph shows the quantization of their respective recovery profiles in wild-type and klp64D^{k1} mutant backgrounds. Contrary to that of GFP::ChAT, the axonal flux of KLP64D::GFP is constitutive and is unaffected by the absence of the tail domain. Both KLP64D::GFP and KLP64D(ΔT)::GFP showed a rescue of *Klp64D^{k1}* allele.

Figure S5: Axonal localization of GFP::Tubulin84B in wild-type and Klp64D^{k1} homozygous larval brain. Confocal images of interneurons from the ventral ganglion (VG) of *Cha-GAL4>UAS-GFP::Tubulin84B/+* (wild-type) and *Cha-GAL4>UAS-GFP::Tubulin84B/+; Klp64D^{k1}* larvae. In both cases, the larvae were aged to 78 h AEL and then the VGs were dissected and mounted on a coverslip for imaging. The images were collected at equal laser power and gain setting using the Olympus FV1000SPD confocal microscope. Images of multiple different interneurons found in the equivalent regions of the wild-type and mutant VGs have been presented for comparison. Scale bar = 10 μm. Comparable localization of GFP::tubulin84B suggests that the axonal channels may not be blocked in the *Klp64D^{k1}* mutant VG.

Table S1: Significance of the differences of recovery of GFP and GFP::ChAT under distinct genetic backgrounds at different time points of observation.

Table S2: List of Antibodies used and their dilutions.

Table S3: List of fly stocks used.

Video S1: GFP::ChAT FRAP in a VG axon shown in 8-bit, false color, intensity heat map (Fire).

Please note: Wiley-Blackwell are not responsible for the content or functionality of any supporting materials supplied by the authors. Any queries (other than missing material) should be directed to the corresponding author for the article.

References

1. Miller KE, Heidemann SR. What is slow axonal transport? Exp Cell Res 2008;314:1981–1990.
2. Hoffman PN, Lasek RJ. The slow component of axonal transport. Identification of major structural polypeptides of the axon and their generality among mammalian neurons. J Cell Biol 1975;66:351–366.
3. Lasek RJ, Paggi P, Katz MJ. Slow axonal transport mechanisms move neurofilaments relentlessly in mouse optic axons. J Cell Biol 1992;117:607–616.
4. Dillman JF 3rd, Dabney LP, Karki S, Paschal BM, Holzbaur EL, Pfister KK. Functional analysis of dynactin and cytoplasmic dynein in slow axonal transport. J Neurosci 1996;16:6742–6752.
5. Rao MV, Engle LJ, Mohan PS, Yuan A, Qiu D, Cataldo A, Hassinger L, Jacobsen S, Lee VM, Andreadis A, Julien JP, Bridgman PC, Nixon RA. Myosin Va binding to neurofilaments is essential for correct myosin Va distribution and transport and neurofilament density. J Cell Biol 2002;159:279–290.
6. Yuan A, Mills RG, Bamburg JR, Bray JJ. Cotransport of glyceraldehyde-3-phosphate dehydrogenase and actin in axons of chicken motoneurons. Cell Mol Neurobiol 1999;19:733–744.
7. Brady ST, Lasek RJ. Nerve-specific enolase and creatine phosphokinase in axonal transport: soluble proteins and the axoplasmic matrix. Cell 1981;23:515–523.
8. Morfini GA, Burns M, Binder LI, Kanaan NM, LaPointe N, Bosco DA, Brown RH Jr, Brown H, Tiwari A, Hayward L, Edgar J, Nave

KA, Garberrn J, Atagi Y, Song Y. Axonal transport defects in neurodegenerative diseases. J Neurosci 2009;29:12776–12786.
9. Wujek JR, Lasek RJ. Correlation of axonal regeneration and slow component B in two branches of a single axon. J Neurosci 1983;3:243–251.
10. Baas PW, Buster DW. Slow axonal transport and the genesis of neuronal morphology. J Neurobiol 2004;58:3–17.
11. Roy S, Coffee P, Smith G, Liem RK, Brady ST, Black MM. Neurofilaments are transported rapidly but intermittently in axons: implications for slow axonal transport. J Neurosci 2000;20:6849–6861.
12. Wang L, Ho CL, Sun D, Liem RK, Brown A. Rapid movement of axonal neurofilaments interrupted by prolonged pauses. Nat Cell Biol 2000;2:137–141.
13. Wang L, Brown A. Rapid intermittent movement of axonal neurofilaments observed by fluorescence photobleaching. Mol Biol Cell 2001;12:3257–3267.
14. Yabe JT, Chan WK, Chylinski TM, Lee S, Pimenta AF, Shea TB. The predominant form in which neurofilament subunits undergo axonal transport varies during axonal initiation, elongation, and maturation. Cell Motil Cytoskeleton 2001;48:61–83.
15. Wang L, Brown A. Rapid movement of microtubules in axons. Curr Biol 2002;12:1496–1501.
16. Roy S, Winton MJ, Black MM, Trojanowski JQ, Lee VM. Rapid and intermittent cotransport of slow component-b proteins. J Neurosci 2007;27:3131–3138.
17. Roy S, Winton MJ, Black MM, Trojanowski JQ, Lee VM. Cytoskeletal requirements in axonal transport of slow component-b. J Neurosci 2008;28:5248–5256.
18. Terada S, Kinjo M, Hirokawa N. Oligomeric tubulin in large transporting complex is transported via kinesin in squid giant axons. Cell 2000;103:141–155.
19. Brown A, Wang L, Jung P. Stochastic simulation of neurofilament transport in axons: the ''stop-and-go'' hypothesis. Mol Biol Cell 2005;16:4243–4255.
20. Trivedi N, Jung P, Brown A. Neurofilaments switch between distinct mobile and stationary states during their transport along axons. J Neurosci 2007;27:507–516.
21. Scott DA, Das U, Tang Y, Roy S. Mechanistic logic underlying the axonal transport of cytosolic proteins. Neuron 2011;70:441–454.
22. Oda Y. Choline acetyltransferase: the structure, distribution and pathologic changes in the central nervous system. Pathol Int 1999;49:921–937.
23. Wooten GF, Cheng CH. Transport and turnover of acetylcholinesterase and choline acetyltransferase in rat sciatic nerve and skeletal muscle. J Neurochem 1980;34:359–366.
24. Baqri R, Charan R, Schimmelpfeng K, Chavan S, Ray K. Kinesin-2 differentially regulates the anterograde axonal transports of acetylcholinesterase and choline acetyltransferase in *Drosophila*. J Neurobiol 2006;66:378–392.
25. Greenspan RJ. Mutations of Choline Acetyltransferase and associated neural defects in *Drosophila melanogaster*. J Comp Physiol 1980;137:83–92.
26. Yasuyama KKT, Salvaterra PM. Differential regulation of choline acetyltransferase expression in the central nervous system of *Drosophila*: a study using temperature-sensitive mutants. Neurosci Res 1996;25:S103–S103.
27. Schliebs R, Arendt T. The cholinergic system in aging and neuronal degeneration. Behav Brain Res 2011;221:555–563.
28. Nyakas C, Granic I, Halmy LG, Banerjee P, Luiten PG. The basal forebrain cholinergic system in aging and dementia. Rescuing cholinergic neurons from neurotoxic amyloid-beta42 with memantine. Behav Brain Res 2011;221:594–603.
29. Tateno M, Kato S, Sakurai T, Nukina N, Takahashi R, Araki T. Mutant SOD1 impairs axonal transport of choline acetyltransferase and acetylcholine release by sequestering KAP3. Hum Mol Genet 2009;18:942–955.
30. Doodhi H, Ghosal D, Krishnamurthy M, Jana SC, Shamala D, Bhaduri A, Sowdhamini R, Ray K. KAP, the accessory subunit of kinesin-2, binds the predicted coiled-coil stalk of the motor subunits. Biochemistry 2009;48:2248–2260.
31. Ray K, Perez SE, Yang Z, Xu J, Ritchings BW, Steller H, Goldstein LS. Kinesin-II is required for axonal transport of choline acetyltransferase in *Drosophila*. J Cell Biol 1999;147:507–518.
32. Pilling AD, Horiuchi D, Lively CM, Saxton WM. Kinesin-1 and Dynein are the primary motors for fast transport of mitochondria in *Drosophila* motor axons. Mol Biol Cell 2006;17:2057–2068.
33. Barkus RV, Klyachko O, Horiuchi D, Dickson BJ, Saxton WM. Identification of an axonal kinesin-3 motor for fast anterograde vesicle transport that facilitates retrograde transport of neuropeptides. Mol Biol Cell 2008;19:274–283.
34. Song AH, Wang D, Chen G, Li Y, Luo J, Duan S, Poo MM. A selective filter for cytoplasmic transport at the axon initial segment. Cell 2009;136:1148–1160.
35. Mitchell CS, Lee RH. A quantitative examination of the role of cargo-exerted forces in axonal transport. J Theor Biol 2009;257:430–437.
36. Berezuk MA, Schroer TA. Dynactin enhances the processivity of kinesin-2. Traffic 2007;8:124–129.
37. Pahud G, Salem N, van de Goor J, Medilanski J, Pellegrinelli N, Eder-Colli L. Study of subcellular localization of membrane-bound choline acetyltransferase in Drosophila central nervous system and its association with membranes. Eur J Neurosci 1998;10:1644–1653.
38. Gabrielle P, Jeana M, Lorenza EC. Cytosolic choline acetyltransferase binds specifically to cholinergic plasma membrane of rat brain synaptosomes to generate membrane-bound enzyme. Neurochem Res 2003;28:543–549.
39. Wedaman KP, Meyer DW, Rashid DJ, Cole DG, Scholey JM. Sequence and submolecular localization of the 115-kD accessory subunit of the heterotrimeric kinesin-II (KRP85/95) complex. J Cell Biol 1996;132:371–380.
40. Kimura T, Watanabe H, Iwamatsu A, Kaibuchi K. Tubulin and CRMP-2 complex is transported via Kinesin-1. J Neurochem 2005;93:1371–1382.
41. Schlager MA, Hoogenraad CC. Basic mechanisms for recognition and transport of synaptic cargos. Mol Brain 2009;2:25.
42. Terada S, Kinjo M, Aihara M, Takei Y, Hirokawa N. Kinesin-1/Hsc70-dependent mechanism of slow axonal transport and its relation to fast axonal transport. EMBO J 2010;29:843–854.
43. Lam H, Matroule JY, Jacobs-Wagner C. The asymmetric spatial distribution of bacterial signal transduction proteins coordinates cell cycle events. Dev Cell 2003;5:149–159.
44. Cheeks RJ, Canman JC, Gabriel WN, Meyer N, Strome S, Goldstein B. C. elegans PAR proteins function by mobilizing and stabilizing asymmetrically localized protein complexes. Curr Biol 2004;14:851–862.
45. Guo M, Jan LY, Jan YN. Control of daughter cell fates during asymmetric division: interaction of Numb and Notch. Neuron 1996;17:27–41.
46. Sannerud R, Marie M, Nizak C, Dale HA, Pernet-Gallay K, Perez F, Goud B, Saraste J. Rab1 defines a novel pathway connecting the pre-Golgi intermediate compartment with the cell periphery. Mol Biol Cell 2006;17:1514–1526.
47. Salvaterra PM, Kitamoto T. *Drosophila* cholinergic neurons and processes visualized with Gal4/UAS-GFP. Brain Res Gene Expr Patterns 2001;1:73–82.
48. Jana SC, Girotra M, Ray K. Heterotrimeric kinesin-II is necessary and sufficient to promote different stepwise assembly of morphologically distinct bipartite cilia in *Drosophila* antenna. Mol Biol Cell 2011;22:769–781.